AGU ADVANCING EARTH AND SPACE SCIENCES

Earth and Space Science

RESEARCH ARTICLE
10.1029/2025EA004350

In Situ Measurements of Ice and Snow Emissivity in the Far-Infrared

L. Warwick[1], H. Oetjen[1], J. Murray[2,3], S. Panditharatne[2,4], H. Brindley[2,3], D. Schuettemeyer[1], X. Chen[5], and X. Huang[5]

[1]ESA-ESTEC, Noordwijk, The Netherlands, [2]Imperial College London, London, UK, [3]National Centre for Earth Observation, Leicester, UK, [4]RAL Space, Chilton, UK, [5]University of Michigan, Ann Arbor, MI, USA

Key Points:

- The Far INfrarED Spectrometer for Surface Emissivity has been deployed in an Arctic environment to measure mid- and far-infrared radiance
- The emissivity of snow and ice were retrieved and agree well with modeled emissivity

Correspondence to:
H. Oetjen,
hilke.oetjen@esa.int

Citation:
Warwick, L., Oetjen, H., Murray, J., Panditharatne, S., Brindley, H., Schuettemeyer, D., et al. (2025). In situ measurements of ice and snow emissivity in the far-infrared. *Earth and Space Science*, *12*, e2025EA004350. https://doi.org/10.1029/2025EA004350

Received 11 APR 2025
Accepted 18 AUG 2025

Author Contributions:
Conceptualization: L. Warwick, H. Oetjen, J. Murray
Formal analysis: L. Warwick, X. Chen, X. Huang
Funding acquisition: H. Oetjen, H. Brindley, D. Schuettemeyer
Investigation: L. Warwick, J. Murray, S. Panditharatne
Methodology: L. Warwick
Project administration: H. Oetjen, H. Brindley, D. Schuettemeyer
Resources: H. Oetjen
Software: X. Chen, X. Huang
Supervision: H. Oetjen, H. Brindley
Visualization: L. Warwick
Writing – original draft: L. Warwick
Writing – review & editing: H. Oetjen, J. Murray, S. Panditharatne, H. Brindley, X. Huang

Abstract This paper describes the first field deployment of the Far INfrarEd Spectrometer for Surface Emissivity far-infrared Fourier transform spectrometer to an Arctic environment and shows retrievals of the emissivity of ice and snow in the wavenumber range 400–1,200 cm^{-1} at viewing angles of 35° and 50°. The retrieved ice emissivity shows a variation of 0.05 between the peak value at around 950 cm^{-1} and the minimum value at around 750 cm^{-1}. The emissivity is also between 0.01 and 0.02 lower for the higher viewing angle. The emissivity of snow is higher and shows less variation with both viewing angle and wavenumber but it is 0.01 less than one below 900 cm^{-1}. This has implications for remote sensing and climate modeling in this wavenumber range as it implies that both the spectral and angular variation of emissivity must be taken into account. The retrieved ice emissivity agrees well with the emissivity modeled using Fresnel equations. The retrieved snow emissivity agrees well with modeled snow emissivity but further independent measurements of the snow physical properties are needed to test the performance of the model in the far infrared.

Plain Language Summary To understand how Earth's climate will change in the future, and to measure Earth's current climate from satellites, it is important to have a good understanding of how Earth's surface absorbs and emits radiation. The property that controls this is called emissivity. However our knowledge of the Earth's emissivity is very limited in a frequency range known as the far-infrared. To fill this gap in our knowledge an instrument was developed that can make emissivity measurements in situ. In this study we describe the use of this instrument in an arctic environment and demonstrate measurements of ice and snow emissivity. Understanding the emissivity of snow and ice is particularly important because this will allow the prediction of how our fragile polar regions will change in a changing climate, for example, by allowing us to accurately predict sea ice cover. Both sets of measurements agree well with theoretical predictions. However it was not possible to rigorously test the model of the snow emissivity because it depends on the size of the snow grains and we could not measure that in this study.

1. Introduction

The emissivity of a surface is the ratio between the electromagnetic radiation emitted by that surface and the radiation it would emit if acting as a blackbody. Every material has its own emissivity which can depend on the angle of emission, wavelength, and microphysical properties. A good knowledge of Earth's surface emissivity is key for understanding Earth's energy budget, which is a vital determinant of Earth's climate and its evolution. This is the balance between the incoming shortwave radiation from the sun and the radiation outgoing from Earth. This outgoing radiation comprises reflected shortwave radiation and longwave radiation that is emitted by Earth. Most of the emitted radiation is in the infrared region of the electromagnetic spectrum between 4 and 100 μm or between 2,500 and 100 cm^{-1} (Wild et al., 2015). Surface emissivity impacts the energy budget because it affects the amount of radiation that is emitted by the Earth's surface. This affects the surface temperature and evaporation of water at the surface and, in spectral regions where the atmosphere is transparent, the energy balance at the top of the atmosphere (Liang et al., 2019). Therefore, in order to model the current and future climate, it is important to have an accurate knowledge of the Earth's emissivity throughout the whole infrared (Feldman et al., 2014; Huang et al., 2016). The spectrally resolved emissivity of the Earth's surface is relatively well known in the mid or thermal infrared (here defined as wavelengths between 4 and 15 μm or wavenumbers between 666 and 2,500 cm^{-1}). This is through retrievals from in situ ground-based measurements (e.g., Langsdale et al., 2020; Salisbury & D'Aria, 1992), satellite instruments such as the Infrared Atmospheric Sounding Interferometer carried on the MetOp satellites (EUMETSAT, 2017), and from laboratory based measurements such as those included in the ECOsystem and Spaceborne Thermal Radiometer Experiment on Space Station spectral library (Meerdink et al., 2019).

There are comparatively few measurements of the Earth's emissivity in the far-infrared (wavelengths longer than 15 μm or wavenumbers less than 666 cm^{-1}) due to difficulties in observing these lower energy photons. These observations are limited to several ground based sets of measurements (Loveless et al., 2024; Palchetti, Barucci, et al., 2020; Warwick et al., 2024) and two sets of retrievals from airborne measurements (Bellisario et al., 2017; Murray et al., 2020). However the situation is changing with the launch of NASA's two CubeSat Polar Radiant Energy in the Far Infrared Experiment (PREFIRE) mission (L'Ecuyer et al., 2021) in 2024 and the planned launch of the European Space Agency's Far-infrared Outgoing Radiation Understanding and Monitoring (FORUM) mission (Palchetti, Brindley, et al., 2020) in 2027. Both missions have an aim of retrieving surface emissivity (Ben-Yami et al., 2022; Xie et al., 2022) leading to the need for validation and accurate a-priori knowledge for retrievals.

The study of ice and snow emissivity is of particular interest as these surface types typically occur in the dry and cold conditions where the atmosphere is most transparent to far-infrared radiation. This means that the far-infrared surface emissivity can have a direct impact on the energy budget at the top of the atmosphere and hence the evolution of the climate (Feldman et al., 2014). It has also been shown that the future evolution of Arctic sea ice and near-surface temperature are sensitive to the representation of far-infrared emissivity (Huang et al., 2016). However, these studies are based on theoretical models of far-infrared emissivity. Observations in the mid-infrared show a strong emissivity sensitivity to snow and ice conditions (Hori et al., 2006) and theoretical studies imply this is also the case for the far-infrared (Chen et al., 2014) but more observations are needed to test these simulation based findings and, if necessary, improve current models of snow emissivity. Finally, these cold and dry atmospheric conditions are the regions that are the key targets for FORUM and PREFIRE surface emissivity retrievals (Ben-Yami et al., 2022; Xie et al., 2022).

To address the lack of in situ far-infrared emissivity measurements the Far INfrarEd Spectrometer for Surface Emissivity (FINESSE) (Murray et al., 2024) and an associated method for retrieving in situ surface emissivity (Warwick et al., 2024) have been developed. This paper builds on that work and aims to: further develop the emissivity retrieval method for application to snow and ice surfaces, make in situ measurements of snow and ice emissivity using FINESSE, and compare these measurements to available emissivity models. This was undertaken as part of larger field deployment to the Arctic circle which aimed to test FINESSE in the field for the first time and to support ESA's FORUM mission by collecting novel data sets including upwelling and downwelling radiance spectra extending into the far-infrared under a range of different atmospheric conditions (European Space Agency, 2024).

2. Instrumentation and the Andøya Measurement Campaign

2.1. The FINESSE Instrument

FINESSE is a Fourier Transform Infrared spectrometer comprising a Bruker EM 27 spectrometer and a custom pointing and calibration system (Murray et al., 2024). The system has a spectral range of 400–1,600 cm^{-1} (6.3–25 μm) and spectral resolution of 0.5 cm^{-1}. The acquisition time for a single interferogram is about 1.5 s. A Fourier Transform is applied to the interferogram to produce a radiance spectrum. The calibration system consists of a heated black body and an ambient temperature black body which are used to perform a two point calibration of the measured radiance. The black bodies are cylindrical cavities with back plates coated in Vantablack® and internal walls painted with Aeroglaze® Z306 paint. The noise equivalent spectral radiance of FINESSE is approximately 1 mW/(m^2 sr cm^{-1}) at 500 cm^{-1}. The calibration error is scene dependent but is at most 2 mW/(m^2 sr cm^{-1}) for cold scenes. The pointing system allows FINESSE to view at any angle from nadir to zenith. The pointing can be controlled and automated via connection to a PC. In addition to measuring the radiance spectra, FINESSE also uses a Vaisala PTU300 pressure, temperature, humidity sensor, and a Vaisala GMP343 CO_2 sensor to monitor atmospheric conditions close to the instrument. FINESSE had been designed to operate in temperatures down to −20°C, and this combined with the low noise equivalent spectral radiance, fast acquisition time, and flexible pointing, make it a suitable choice for the retrieval of emissivity in Arctic conditions. For a more detailed description of FINESSE including photographs of the instrument and details about the processing of interferograms to calibrated radiance measurements, see Murray et al. (2024).

10.1029/2025EA004350

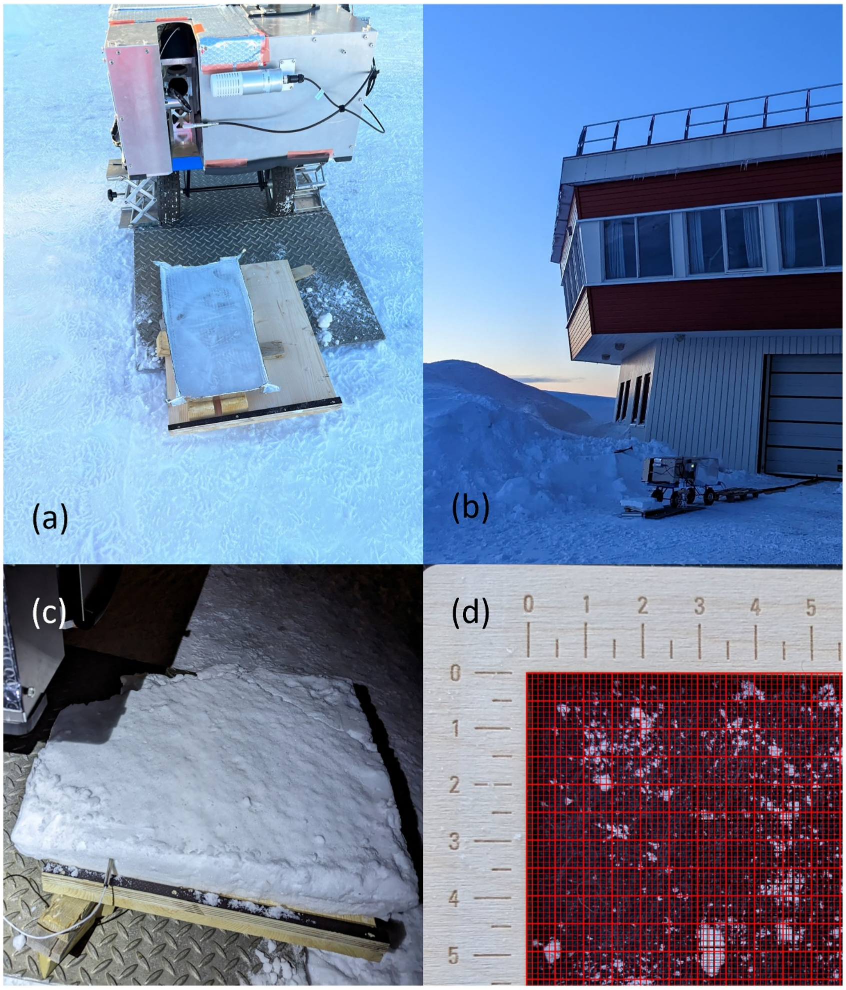

Figure 1. (a) The setup for the ice emissivity measurements. (b) The setup for the snow emissivity measurements. (c) The snow sample. (d) Snow crystals from the top of the snow sample. The pictured scale is in cm and a 1 × 1 mm grid is overlayed in red.

2.2. The Andøya Campaign and Data Collection

FINESSE was deployed to the ALOMAR Observatory, Andøya Space, Andenes, Norway (69°16′ N, 16°0′ E, 372 m above sea level) between 6 February and 17 March 2023. This deployment was funded by the European Space Agency and facilitated by support from the MC2-ICEPACKS campaign organized by the University of Oslo. As part of this deployment measurements of the emissivity of an ice and a snow sample were taken overnight on 8 March 2023 between 01:00 and 07:30 UTC. This time was selected for measurements because of the cold dry conditions and clear skies. Figures 1a and 1b show the setup for the ice and snow measurements respectively.

The ice sample was prepared by placing water outside to freeze in a plastic tray. The final dimensions of the ice sample were roughly 50 × 30 cm and the ice had a depth of several cm. For the emissivity measurements, the ice sample was placed a distance of 48 cm below the base of FINESSE and leveled with a spirit level. For the snow, a flat sample with a surface area of roughly 50 × 50 cm and a depth of around 20 cm was cut from a nearby snow drift. For the emissivity measurements, this was placed 24 cm below the base of FINESSE and leveled with a spirit level. Figure 1c shows the snow sample. Crystals from the top layer were photographed. The crystals were gently brushed onto a black felt background and photographed with a ruler for scale. Figure 1 shows one of these photographs with a 1 × 1 mm grid overlayed.

To retrieve surface emissivity measurements using the method described in Warwick et al. (2024) measurements must be made of the radiation upwelling from the surface under study and of the radiation downwelling from the atmosphere onto the sample. This is to account for both the radiation emitted and reflected by the sample. FINESSE makes these radiance measurements in cycles that consist of scene views and views of the hot and cold calibration targets. For this study each measurement cycle consisted of 3 scene views, 2 of the surface under study and one of the sky, and 4 calibration views. This meant that each measurement cycle lasted around 7 min and multiple scene views allowed for averaging to improve the signal-to-noise ratio. The samples were viewed at angles of 35° and 50°, chosen to examine the angular dependence of the emissivity with the lower angle of 35° chosen to avoid the shading of the sample by FINESSE. The viewing angle was changed every 5 measurement cycles. In total 10 measurement cycles were completed for the ice sample resulting in around 70 min of measurements and 30 measurement cycles were completed for the snow sample consisting of around 210 min of measurement. Measurements of the pressure, temperature, humidity, and CO_2 concentration at the level of the instrument were made throughout the measurement cycles. The atmospheric conditions were clear and cold with an air temperature between −11°C and −8°C and a humidity of between 60% and 75%.

3. Emissivity Retrieval Method

The emissivity retrieval method is developed from that described in Warwick et al. (2024), which is adapted from previous work in the mid-infrared (Fiedler & Bakan, 1997; Newman et al., 2005; Smith et al., 1996) and far-infrared (Bellisario et al., 2017; Loveless et al., 2024; Murray et al., 2020). In Warwick et al. (2024) the emissivity of a specular surface was found using

$$\epsilon = \frac{L_{\text{det}}^{\uparrow} - \tau^2 L_{\text{det}}^{\downarrow} - \left(1 - \tau^2\right) B(T_a)}{\tau\{B(T_s) - \tau L_{\text{det}}^{\downarrow} - (1 - \tau) B(T_a)\}}. \tag{1}$$

where ϵ is the emissivity, $L_{\text{det}}^{\uparrow}$ the upwelling radiance measured by FINESSE, τ the transmission between the surface and FINESSE, $L_{\text{det}}^{\downarrow}$ the downwelling radiance measured by FINESSE, $B(T_a)$ the Planck function at the temperature of the near surface atmosphere and $B(T_s)$ the Planck function at the temperature of the surface. However, this equation can only be applied for surfaces that act as specular reflectors due to the assumption made that the incident angle of the downwelling radiation is equal to the viewing angle. It also makes the assumption that the emission of the atmospheric layer between the surface and FINESSE can be approximated using

$$(1 - \tau(\theta)) B(T_a) \tag{2}$$

which does not hold in regions of saturated atmospheric absorption. Therefore, for this study Equation 1 was re-derived without these two assumptions. In addition, the temperature retrieval method was updated from that used in Warwick et al. (2024) to make the method more robust for use in a wider range of atmospheric conditions. This updated temperature retrieval method can be used for both specular and non-specular surfaces.

Figure 2 shows the geometry of the updated retrieval method and Figure 3 summarizes the data required and processing steps.

The spectrally resolved upwelling radiation at the surface at an angle of θ_1 degrees, $L_{\text{surf},\theta_1}^{\uparrow}(\nu)$, is given by

$$L_{\text{surf},\theta_1}^{\uparrow}(\nu) = \epsilon_{\theta_1}(\nu) B(T_s)(\nu) + (1 - \epsilon_{\theta_1}(\nu)) L_{\text{surf},\theta_2}^{\downarrow}(\nu) \tag{3}$$

where $\epsilon_{\theta_1}(\nu)$ is the emissivity at wavenumber ν and viewing angle θ_1, $B(T_s)(\nu)$ the Planck function at the surface temperature T_s, and $L_{\text{surf},\theta_2}^{\downarrow}(\nu)$ is the downwelling radiation at the surface that is reflected into the field of view of FINESSE. For this analysis, this radiation is represented by the radiation at a single angle θ_2.

$L_{\theta_1}^{\uparrow}(\nu)$, the upwelling radiation at the spectrometer is related to the upwelling radiation at the surface by

$$L_{\theta_1}^{\uparrow}(\nu) = \tau_{\theta_1}(\nu) L_{\text{surf},\theta_1}^{\uparrow}(\nu) + L_{\theta_1}^{\text{layer}}(\nu) \tag{4}$$

10.1029/2025EA004350

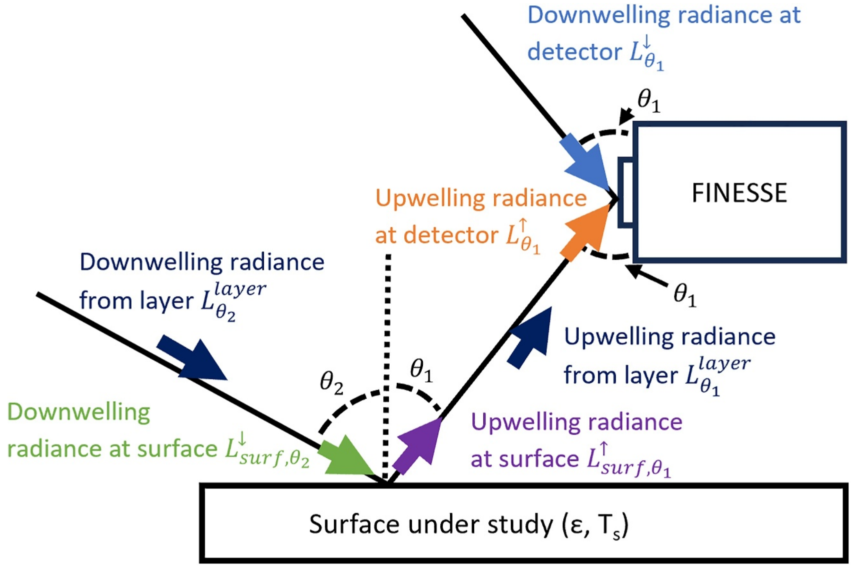

Figure 2. Schematic showing the geometry of the retrieval method.

where $\tau_{\theta_1}(\nu)$ is the transmission of the atmospheric layer between the surface and the spectrometer at an angle of θ_1 and $L^{\text{layer}}_{\theta_1}(\nu)$ is the emission from the layer at an angle of θ_1.

Similarly, the downwelling radiation at the surface $L^{\downarrow}_{\text{surf},\theta_2}(\nu)$ is given by

$$L^{\downarrow}_{\text{surf},\theta_2}(\nu) = \tau_{\theta_2}(\nu) L^{\downarrow}_{\theta_2}(\nu) + L^{\text{layer}}_{\theta_2}(\nu) \tag{5}$$

where $\tau_{\theta_2}(\nu)$ is the transmission through the layer, $L^{\downarrow}_{\theta_2}(\nu)$ is the downwelling radiation at the spectrometer and $L^{\text{layer}}_{\theta_2}(\nu)$ is the emission of the layer, all at an angle of θ_2.

By combining Equations 3–5 and rearranging, the emissivity is given by

$$\epsilon_{\theta_1} = \frac{L^{\uparrow}_{\theta_1} - \tau_{\theta_1}\tau_{\theta_2}L^{\downarrow}_{\theta_2} - \tau_{\theta_1}L^{\text{layer}}_{\theta_2} - L^{\text{layer}}_{\theta_1}}{\tau_{\theta_1}\{B(T_s) - \tau_{\theta_2}L^{\downarrow}_{\theta_2} - L^{\text{layer}}_{\theta_2}\}}. \tag{6}$$

For legibility, the dependence on wavenumber has been omitted.

When measuring the emissivity of a surface such as flat water or ice that acts as a specular reflector, the angles θ_1 and θ_2 can be assumed to be the same and the equation simplifies to:

$$\epsilon_{\theta_1} = \frac{L^{\uparrow}_{\theta} - \tau^2_{\theta}L^{\downarrow}_{\theta} - \tau_{\theta}L^{\text{layer}}_{\theta} - L^{\text{layer}}_{\theta}}{\tau_{\theta}\{B(T_s) - \tau_{\theta}L^{\downarrow}_{\theta} - L^{\text{layer}}_{\theta}\}}. \tag{7}$$

However, the assumption of specular reflection does not hold for snow surfaces. In this case the downwelling radiance is an integral over the hemisphere defined by the snow surface, modified by the hemispherical–directional reflectance factor which describes the proportion of downwelling radiance from each angle that is reflected into the field of view of FINESSE (Schaepman-Strub et al., 2006). For this study, we follow the method of Bellisario et al. (2017) and Loveless et al. (2024) and assume that the snow surface acts as a Lambertian reflector. Therefore, provided there is an uninterrupted view to the horizon, the downwelling radiation can be approximated by the downwelling radiation measured at a representative angle, usually 55°. If this representative angle is not directly measured then a correction factor, γ_{θ}, can be calculated using simulated radiances where

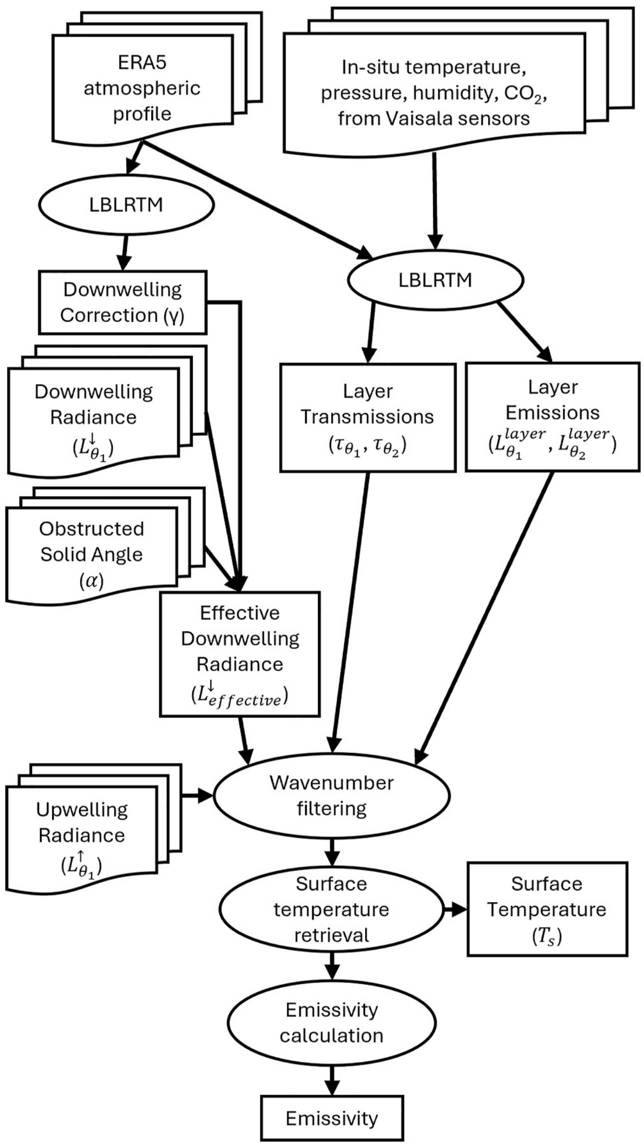

Figure 3. A summary of the inputs and processing steps required to retrieve emissivity.

$$\gamma_{\theta_{a,55}} = \frac{L^{\downarrow}_{\theta_{55}}}{L^{\downarrow}_{\theta_a}}. \tag{8}$$

Here $L^{\downarrow}_{\theta_{55}}$ is the downwelling radiation simulated at 55° and $L^{\downarrow}_{\theta_a}$ is the downwelling radiation simulated at the measured angle (Borbas et al., 2021; Loveless et al., 2024). This means that the emissivity of a surface that acts as a Lambertian reflector can be found using

$$\epsilon_{\theta_1} = \frac{L^{\uparrow}_{\theta_1} - \tau_{\theta_1}\tau_{\theta_2}\gamma L^{\downarrow}_{\theta_1} - \tau_{\theta_1}L^{\text{layer}}_{\theta_2} - L^{\text{layer}}_{\theta_1}}{\tau_{\theta_1}\{B(T_s) - \tau_{\theta_2}\gamma L^{\downarrow}_{\theta_1} - L^{\text{layer}}_{\theta_2}\}}. \tag{9}$$

However, if the view to the horizon is interrupted, for example, by a building, then this must also be accounted for in the downwelling radiance. This can be approximated by estimating the fraction of solid angle subtended by the obstruction, α, and making the assumption that the object radiates as a blackbody at the near-surface atmospheric temperature. The effective downwelling radiance, $L^{\downarrow}_{\text{effective}}$, can then be found using

$$L^{\downarrow}_{\text{effective}} = (1-\alpha)\gamma L^{\downarrow}_{\theta_1} + \alpha B(T_a), \tag{10}$$

making the final emissivity equation,

$$\epsilon_{\theta_1} = \frac{L^{\uparrow}_{\theta_1} - \tau_{\theta_1}\tau_{\theta_2}L^{\downarrow}_{\text{effective}} - \tau_{\theta_1}L^{\text{layer}}_{\theta_2} - L^{\text{layer}}_{\theta_1}}{\tau_{\theta_1}\{B(T_s) - \tau_{\theta_2}\gamma L^{\downarrow}_{\text{effective}} - L^{\text{layer}}_{\theta_2}\}}. \tag{11}$$

When retrieving surface emissivity, the up and downwelling radiance at the spectrometer can be measured directly, the surface temperature can be determined from the radiance measurements but the transmission and emission of the atmospheric layer between the surface and instrument must be modeled.

3.1. Radiative Transfer Calculations

For these measurements, the transmission of the atmospheric layer between the surface and FINESSE was modeled using the Line by Line Radiative Transfer Model (LBLRTM) version 12.15 in horizontal mode (Clough et al., 2005). This was done individually for each 7 min measurement cycle using the temperature, pressure, humidity, and CO_2 concentration recorded by FINESSE's environmental monitoring instruments averaged over that 7 min. The concentration of ozone was taken from the ERA5 reanalysis at the pressure level measured by FINESSE's sensor (Hersbach et al., 2023). The total path length for the simulations was 0.483 m for the ice surface and 0.395 m for the snow surface. The transmission was calculated with a spectral resolution of 0.01 cm^{-1} and apodized with the FINESSE instrument line shape (Murray et al., 2024). Figure 4a shows an example of the calculated transmission for each viewing angle. Even over the short path length, the modeling using LBLRTM shows significant absorption by CO_2 at 667 cm^{-1} (15 μm) and absorption by water vapor below 550 cm^{-1} and above 1,350 cm^{-1} (above 20 μm and below 7.5 μm). The variation of the transmission was at most 1% during the course of the measurements.

For the snow surface, surface correction factors were calculated using Equation 8. To do this, the downwelling radiation was simulated using LBLRTM at angles of 55°, 50°, and 35°. The surface values for pressure, temperature, humidity, and CO_2 measured by FINESSE and the atmospheric profiles from ERA5 (Hersbach et al., 2023) at the nearest grid point in space and time to the measurements were used as input. Figure 4b shows

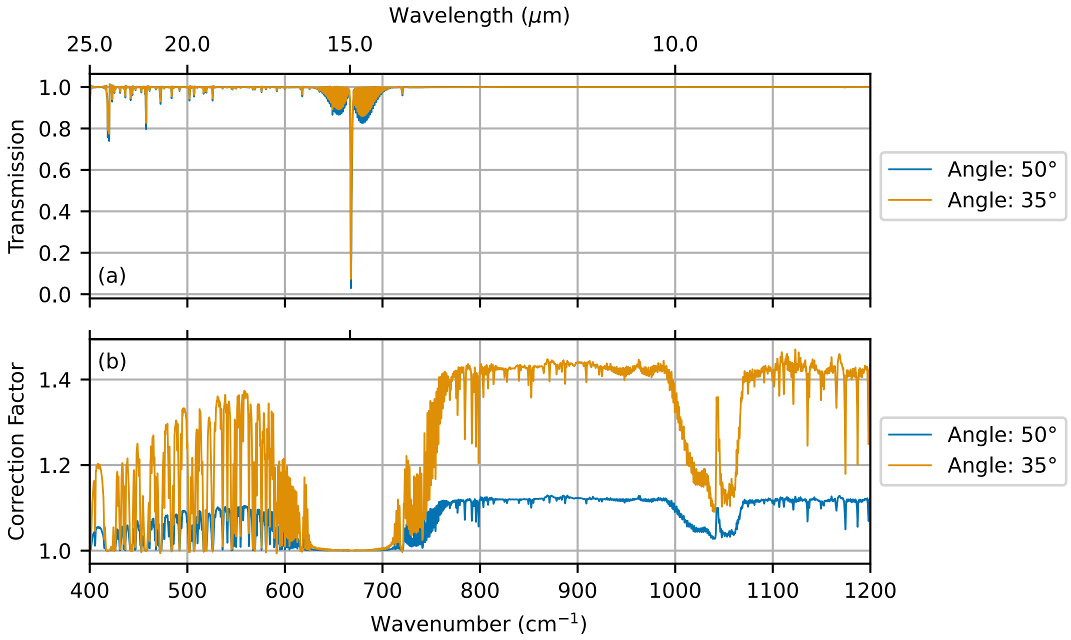

Figure 4. (a) Examples of the transmission through the atmosphere between the surface and Far INfrarEd Spectrometer for Surface Emissivity for the 35° and 50° viewing angles calculated using the Line-by-line Radiative Transfer Model. (b) Examples of the correction factors calculated for the 35° and 50° viewing angles.

these correction factors for each viewing angle. The correction factor is higher for the 35° view and for both angles it is higher in regions of higher atmospheric transmission.

3.2. Determination of Surface Skin Temperature

Following Warwick et al. (2024), the radiance measurements were filtered to only retrieve the surface temperature and calculate the emissivity in spectral regions where there was a good contrast between the upwelling and downwelling radiation. This was done by filtering for regions of the spectrum where the upwelling radiation was more than 3 mW/(m^2 sr cm^{-1}) higher than the downwelling radiation. 3 mW/(m^2 sr cm^{-1}) was chosen as it is the sum of the NESR and calibration error.

The surface skin temperature was determined using a method based on that used by Murray et al. (2020), Warwick et al. (2024), and Loveless et al. (2024). This method relies on the fact that emissivity is a smooth function of wavenumber and that the surface temperature is constant across the wavenumber range (Salvaggio & Miller, 2001). Therefore, the best estimate of the surface temperature can be determined by calculating the emissivity for a range of surface temperatures and picking the value that gives the smoothest emissivity retrieval, that is an emissivity retrieval without sharp atmospheric absorption lines. Figure 5a shows an example of ice emissivity calculated using Equation 1 with three input temperatures, and the rest of the parameters kept the same. Three temperatures are chosen as an illustration, but for the actual retrieval the emissivity is calculated every 0.01 K in a range of 10 K. In this case a surface temperature of −7.3°C gives the smoothest emissivity and best compensation for the atmospheric absorption lines.

To quantify the spectral smoothness, the spectral range was divided into sections with a spectral width of 40 cm^{-1}. 40 cm^{-1} was chosen for consistency with the water retrievals of Newman et al. (2005) and Warwick et al. (2024). Within each 40 cm^{-1} section, the emissivity was calculated for a range of surface temperatures. The spectral smoothness for each surface temperature was then the standard deviation of the difference between the calculated emissivity and a quadratic fit of the calculated emissivity. Figure 5b shows the calculated standard deviation as a function of the input surface temperature with different colored curves representing different wavenumber bins. The minima of the curves clustered around a common value, but, as Loveless et al. (2024) also noted, some curves were steeper than others. These steeper curves corresponded to wavenumber bins in the far-infrared where there is more spectral structure. A steeper curve allows for a more precise determination of the surface temperature. In

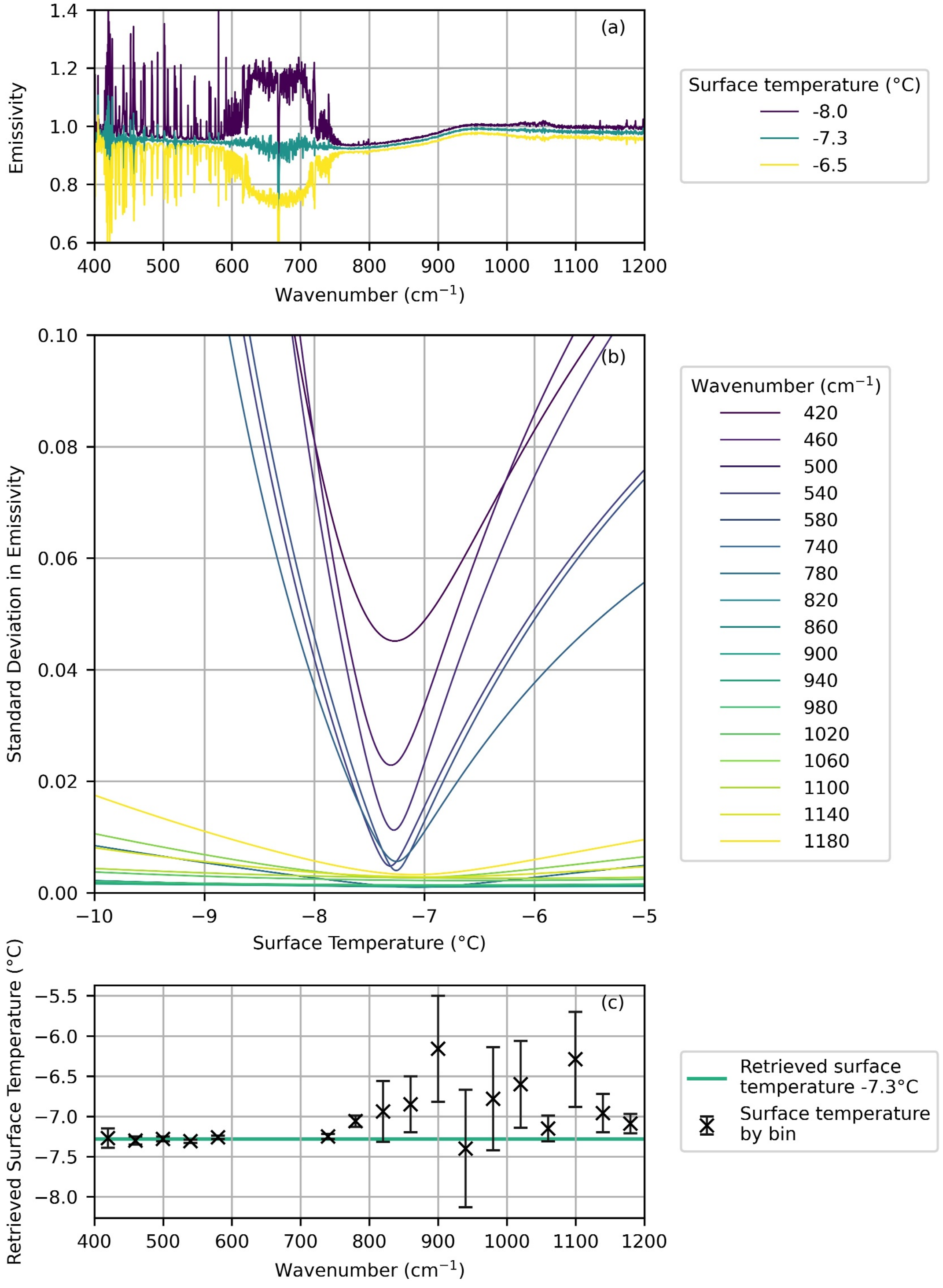

Figure 5. An example of the surface temperature retrieval for an ice surface. (a) Shows the effect of calculating emissivity with a range of surface temperatures. The best estimate of the surface temperature is 7.3°C which produces the smoothest emissivity. In panel (b) the different colors represent different wavenumber bands and the standard deviation is a measure of the smoothness of the retrieval. The minima of the curves are clustering around a common temperature which is the best estimate of the surface temperature. The process for determining the curve width is also shown. (c) The retrieved surface temperature in each wavenumber section as a function of wavelength. The error bars show the curve width. The retrieved surface temperature is shown by the horizontal line.

contrast, above 800 cm^{-1} changing the input surface temperature has a much smaller effect on the smoothness of the emissivity retrieval (see Figure 5a) due to the lack of atmospheric lines in this region of the spectrum. This leads to more variation in the locations of the curve minima in Figure 5b and shallower curves. The steepness of the curves was quantified using a method similar to that proposed by Loveless et al. (2024) where the "curve width" was calculated as the change in input surface temperature required to increase the standard deviation by 1.5%. As the curve width is a relative measurement, the value of 1.5% is arbitrary. However, changing the value leads to a change in retrieved surface temperature an order of magnitude lower than the total uncertainty in the retrieved temperature. Figure 5b shows a graphical representation of the determination of the curve width. Figure 5c shows the retrieved surface temperature in each 40 cm^{-1} bin with the error bars showing the corresponding curve width. The final retrieved surface temperature was then calculated as the average of the retrieved surface temperatures in each 40 cm^{-1} bin, weighted by

$$\frac{1}{(\text{curve width})^2}. \tag{12}$$

The final retrieved surface temperature for this example is shown by the horizontal line in Figure 5c. As expected from the sensitivity of the emissivity to changes in surface temperature shown in Figure 5a and the widths of the curves in Figure 5b, the far-infrared portion of the spectrum has a larger influence on the final retrieved surface temperature.

3.3. Uncertainty Analysis

The uncertainty in the retrieved emissivity and surface temperature was found by perturbing each of the input parameters to Equation 11 and then rerunning the full temperature and emissivity retrieval, following the same procedure described in Warwick et al. (2024). For both the ice and snow samples, the applied perturbations were: the FINESSE NESR and calibration uncertainty; the uncertainty in the transmission between FINESSE and the surface caused by both the measurement error of the Vaisala PTU300 and GMP343 and the atmospheric variability over each 7 min cycle; and the uncertainty in the surface temperature retrieval, determined by the uncertainty in the fit of the retrieved surface temperature.

For the snow case we considered two additional sources of uncertainty. The first was an uncertainty of 5° in the angle of the simulated downwelling correction, chosen to cover the range of suggested values in literature (Bellisario et al., 2017). The second source of uncertainty was uncertainty in the proportion of the sky view that was obstructed by the ALOMAR observatory. The unperturbed emissivity value was calculated assuming that this proportion was zero. Given the size of the observatory and distance from the snow sample, the uncertainty in emissivity was calculated using an obstructed proportion of 20%.

The total uncertainty in the surface temperature was the change in surface temperature caused by each perturbation added in quadrature. Likewise the total uncertainty in emissivity was the change in retrieved emissivity caused by each perturbation added in quadrature.

4. Results and Discussion

4.1. Surface Temperature

Figure 6 shows the measured air temperature and retrieved surface temperature. The error bars show the uncertainty determined in Section 3.3. The retrieved snow surface temperature was cooler than the air temperature and fluctuated rapidly over a range of around 3°C during the course of the measurements, matching the fluctuations in the air temperature. The fast acquisition time of FINESSE allowed the fluctuations to be resolved. The ice surface was warmer than the air temperature and the temperature retrieved at each angle decreased with time. This indicated that the ice sample had not yet reached equilibrium with the outside environment and was still cooling when the measurements were undertaken. Some liquid water was also visible below the ice surface however the ice was sufficiently thick that it would have been opaque to the infrared radiation. The temperature retrievals at 35° were around 4°C warmer than the earlier retrievals at 50°. This could either have been an artifact of the retrieval method that occurs when undertaking retrievals at a range of angles or it could have been caused by FINESSE viewing two different parts of the ice sample with two different surface temperatures. Later

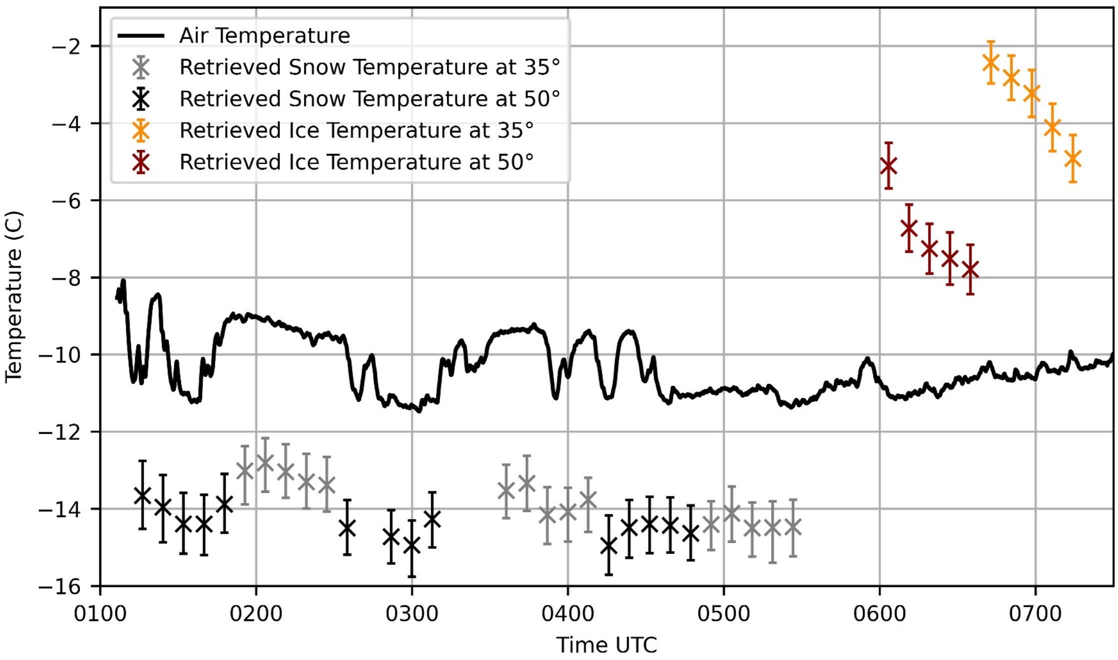

Figure 6. The retrieved surface temperature for the snow (black/gray) and ice (red/orange) retrievals. The solid black line shows the near surface air temperature recorded by FINESSE's PTU300.

investigation of a different ice sample indicated the presence of liquid water under only part of the ice sample could cause this magnitude of temperature variation. However, in this case, since there were no independent surface temperature measurements, it was not possible to determine which explanation was correct. This should be investigated through further measurements of ice emissivity at a variety of angles in combination with independent measurements of the surface temperature, for example, by using a thermal camera.

4.2. Retrieved Emissivity

Figure 7 shows the retrieved emissivity for the ice and snow samples. The error bars show the results of the uncertainty analysis described in Section 3.3. The ice sample shows a variation of around 0.07 over the spectral range and a measurable angular dependence. The emissivity of ice is temperature dependent (Wang et al., 2024) however the difference in emissivity with view angle is much larger than the difference in emissivity expected due to the different surface temperatures retrieved for the two viewing angles. Therefore the difference in emissivity can be attributed to the viewing geometry. This has implications for FORUM and PREFIRE because the surface topography and view angle will affect the surface emissivity. This could impact both the surface emissivity and atmospheric retrievals from these satellites and should be investigated further. There is a much smaller variation in emissivity with wavenumber for the snow sample but the emissivity of the snow is below one at wavenumbers lower than 900 cm^{-1}. There is a suggestion that the emissivity depends on viewing angle, particularly around 800 cm^{-1}, however this variation is smaller than the measurement uncertainty.

Figure 8 shows the uncertainty for the emissivity retrievals separated by source of uncertainty. The downwelling correction and obstruction correction are only applied to the diffusely reflecting snow surface. The assumed uncertainty in these corrections makes the largest contribution to the total uncertainty associated with the snow emissivity retrievals. This suggests that the snow emissivity retrieval could be most easily improved by better control or characterization of the downwelling radiance, for example, by shielding the sample from buildings. The next largest source of uncertainty for the snow case, and the largest source of uncertainty for the ice case is the NESR. This increases significantly below 500 cm^{-1} and also increases above 1,000 cm^{-1} and suggests that the uncertainty in the retrieval could be reduced by measuring for a longer period of time given stable conditions.

10.1029/2025EA004350

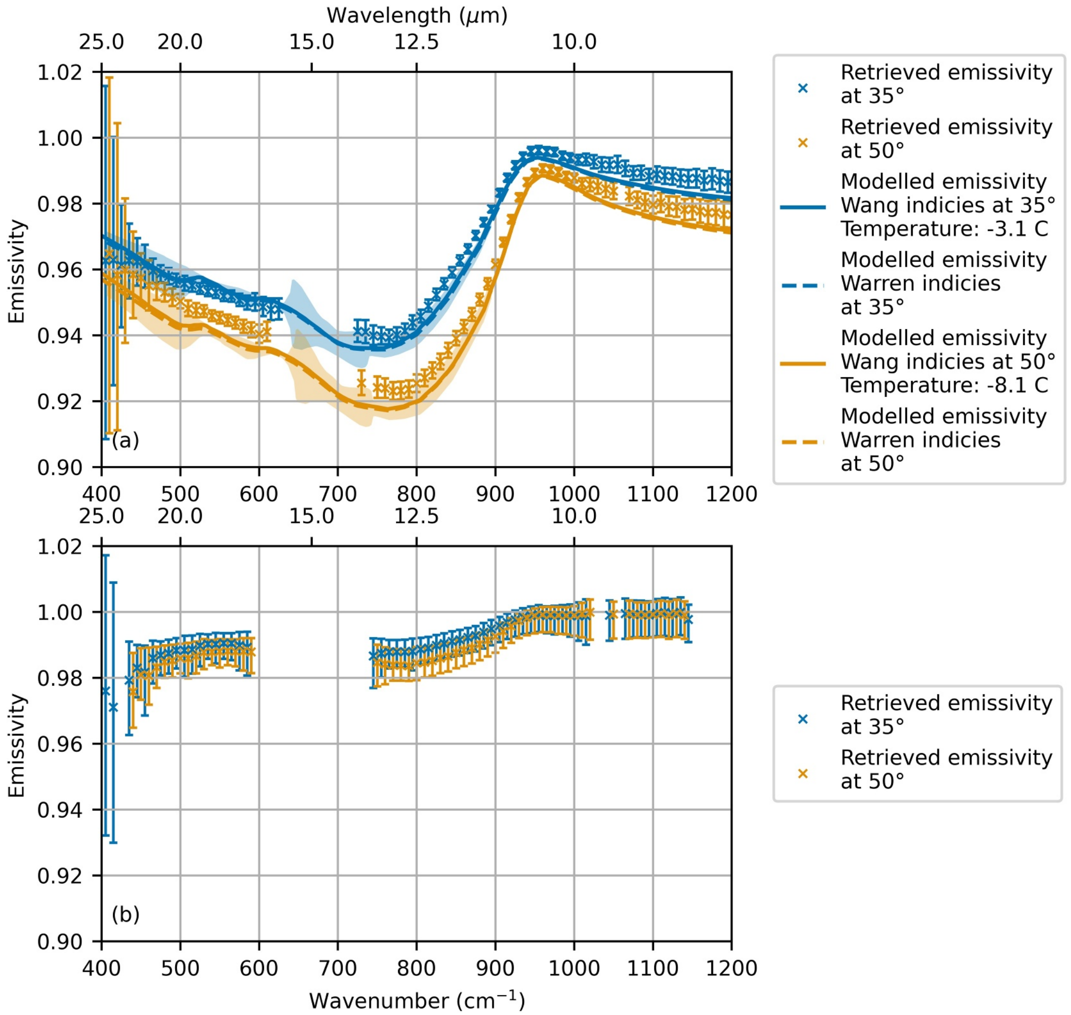

Figure 7. (a) Retrieved ice emissivity at viewing angles of 35° and 50°. The error bars show the uncertainty calculated in Section 3.3. The solid lines and shading show the modeled emissivity calculated using the refractive indices of Warren and Brandt (2008) and the dashed lines show the emissivity modeled using the temperature depended refractive indices from Wang et al. (2024). (b) The retrieved snow emissivity with the uncertainty calculated in Section 3.3.

5. Comparison to Modeling

5.1. Ice

The emissivity of a spectral reflector such as flat ice can be modeled using Fresnel equations, as long as the complex refractive indices are known (Masuda et al., 1988). In this case the reflectance, ρ, which is 1 minus the emissivity, can be calculated based on the viewing angle and refractive index:

$$\rho(n,\theta) = \frac{\left(\left|r_{\|}(n,\theta)\right|^{2} + \left|r_{\perp}(n,\theta)\right|^{2}\right)^{2}}{2}, \tag{13}$$

where n is the complex refractive index, θ is the viewing angle, and $r_{\|}$ and $r_{\perp}$ are the complex reflectances polarized parallel and perpendicular to the plane of incidence. These are given by:

$$r_{\|} = -\frac{n\cos\theta - \cos\theta'}{n\cos\theta + \cos\theta'}, \tag{14}$$

10.1029/2025EA004350

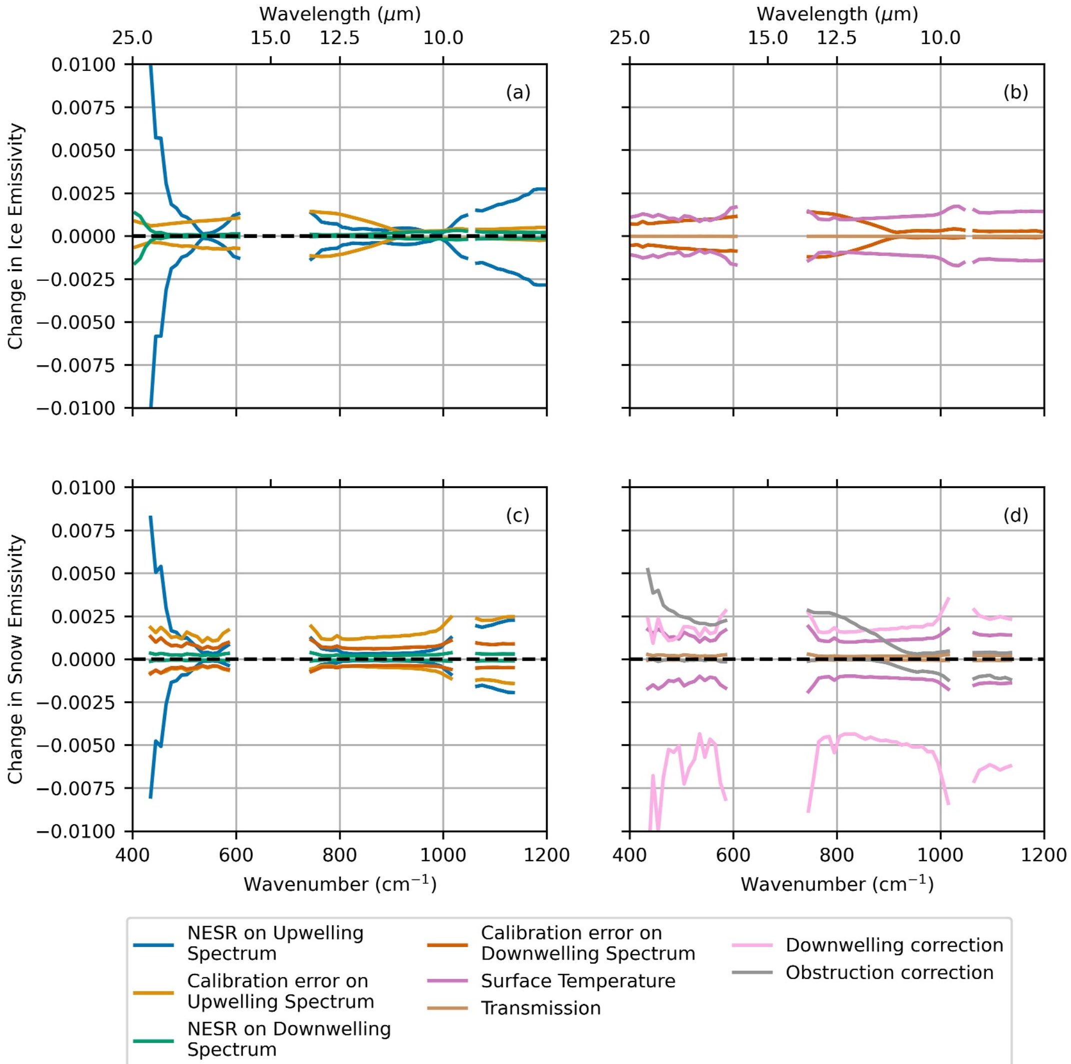

Figure 8. The uncertainty in emissivity found by perturbing each of the input parameters to Equation 6. (a, b) Show the ice case and (c, d) show the snow case.

$$r_{\perp} = \frac{\cos\theta - n\cos\theta'}{\cos\theta + n\cos\theta'}, \tag{15}$$

where θ' is the angle of refraction and is related to θ by

$$\sin\theta' = \frac{1}{n}\sin\theta. \tag{16}$$

Figure 7a shows the retrieved emissivity compared to the emissivity calculated using the refractive indices of Warren and Brandt (2008) and Wang et al. (2024). The Wang et al. (2024) refractive indices are temperature dependent and so have been plotted at the average retrieved surface temperature for each view angle. The shading around the lines represents the uncertainty in the modeled emissivity caused by the uncertainty in the Warren and Brandt (2008) refractive indices. The two sets of refractive indices produce modeled emissivities that are almost identical. The modeled and retrieved emissivity agree well with a maximum difference of 0.005 at 1,200 cm^{-1}. The spectral and angular variation of the emissivity is well captured. Above 1,000 cm^{-1} for both viewing angles and around 550 cm^{-1} for the 50° viewing angle the difference between the modeled and retrieved emissivity is greater than the total uncertainty in the retrieved emissivity calculated in Section 3.3; however, it should be noted

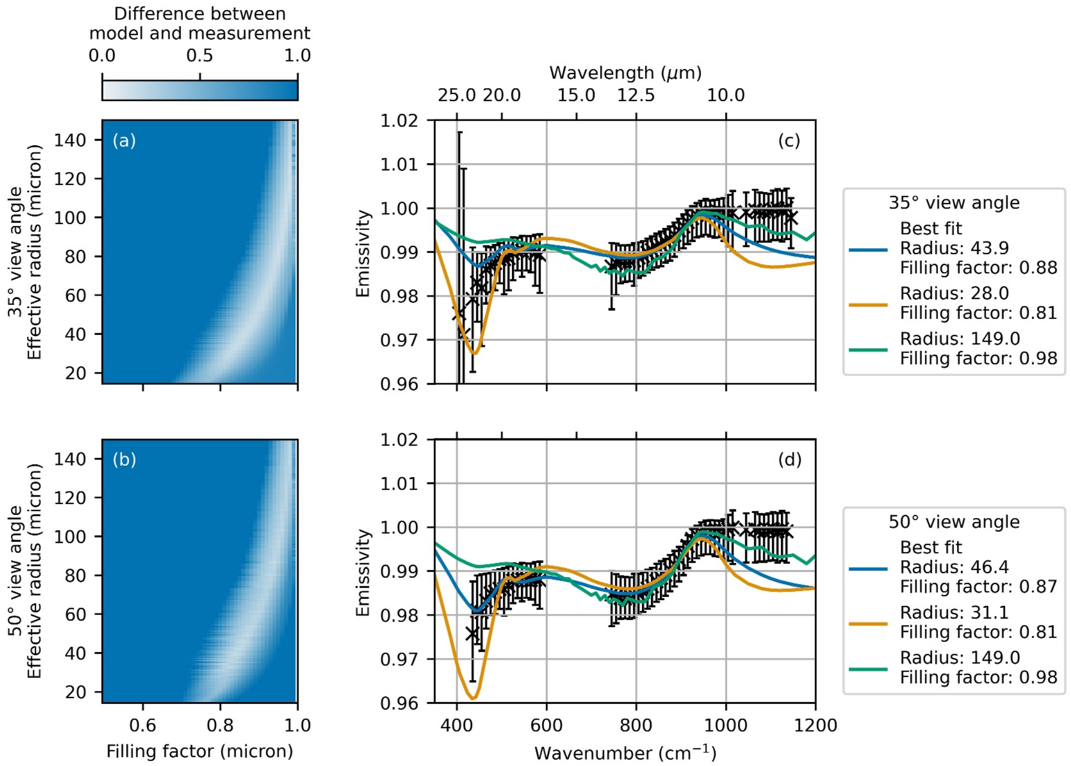

Figure 9. (a, b) The average difference between the modeled and measured emissivity for different values of filling factor and effective radius. Panel (a) shows the 35° viewing angle and panel (b) shows 50°. (c, d) The measured and modeled emissivity for a range of radii and filling factors. Panel (c) shows the 35° viewing angle and (d) shows 50°.

that these uncertainties in the retrieved emissivity represent an uncertainty of 1 standard deviation in the input parameters. A possible explanation for this could be the surface roughness increasing the emissivity of the ice sample (Masuda et al., 1988).

5.2. Snow

For snow surfaces, this paper uses the model of snow emissivity developed by Chen et al. (2014) that is incorporated into the Huang et al. (2016) emissivity database. The inputs to the snow emissivity model are the snow effective grain size and the filling factor. The model calculates the single-scattering parameters for the snow grains based on the assumption that the particles have the refractive indices of ice, are spherical and their sizes are distributed log-normally. The optical properties are calculated using Mie theory and then a "static structure factor" correction is applied that accounts for the dense packing of the grains (Mishchenko, 1994; Mishchenko & Macke, 1997). The resultant single-scattering parameters are then used as input to the Hapke (1993) emissivity model.

This is sufficient to model small snow grain sizes, but for large snow grain sizes the effect of surface welding is also taken into account. This is done by calculating the emissivity twice, once using the method for small snow grains and once using the Fresnel equations for specular reflectance. The output is a weighted average of the emissivity calculated using both methods with the weighting chosen so that the resulting emissivity matched the mid-infrared emissivity measured by Hori et al. (2006).

The snow emissivity calculated using the model was compared to the retrieved snow emissivity for a range of filling factors and effective radii. Figure 9 shows the difference between the retrieved and modeled emissivity for each combination of model input parameters for each viewing angle. This was done by calculating the absolute difference between the retrieved and modeled emissivity and dividing this by the retrieval uncertainty. This was then averaged over the spectral range to give the values shown in Figures 9a and 9b. There were a range of model inputs that resulted in similar agreement with the measurements. These ranged from solutions with a low effective radius and low filling factor to solutions with a higher filling factor and effective radius. Figures 9c and 9d show the best-fit emissivity and two other examples of modeled emissivity that illustrate the range of plausible parameters. The top row shows the 35° view angle and the bottom row shows the 50° view angle.

There was good agreement between the best fit parameters for the two view angles with an average effective radius of 45 microns and filling factor of 0.87 microns. This was expected as the same snow sample was viewed at both angles. These parameters suggested the sample was dense snow with small crystals. This crystal size agreed qualitatively with the small crystals seen in Figure 1d, however the photographs taken of the snow surface did not have sufficient resolution to provide an independent constraint on crystal size. It should also be noted that no combination of input parameters could match the measured emissivity across the whole spectral range. The largest differences were seen above 1,000 cm^{-1} where the measured snow emissivity was higher than the modeled emissivity. This has been observed previously when comparing this model to the measurements of Hori et al. (2006). One possible explanation for this difference could be that the emissivity retrieval method assumes a constant penetration depth and therefore skin temperature across the spectral range of FINESSE. However, change of skin temperature with depth was ruled out as a possible cause for the difference as the penetration depth of the radiation only varies by approximately 30 microns over this spectral range. This meant that the temperature gradient required to match the measurements with the model was unrealistically high. However we can't rule out other penetration depth related effects. From the modeling perspective, differences may be due to assumptions about the snow grain sizes and shapes used in the calculation. The mie-scattering approach assumes spherical particles which may not be realistic enough. Alternatively, the static structure factor, which is used to account for the packing of the grains, becomes weaker as the wavenumber increases which may contribute to the difference seen. However further investigation is required to understand these differences fully.

6. Conclusions and Next Steps

In conclusion this paper demonstrates the retrieval of snow and ice emissivity in the wavenumber range 400–1,200 cm^{-1}. This was carried out using data taken during the first deployment of the recently developed FINESSE instrument to an Arctic environment. This demonstrates that FINESSE can perform well under harsh Arctic operating conditions, highlighting its suitability for further deployments to similar locations. The retrieval of snow emissivity required the improvement of the emissivity and temperature retrieval methods beyond those described in Warwick et al. (2024). This method is now ready to be applied to emissivity measurements from a variety of targets under a broad range of atmospheric conditions.

The retrievals of ice emissivity agree well with simulated emissivity calculated using the refractive indices of Warren and Brandt (2008) and Wang et al. (2024) and show clear variation with both wavenumber and viewing angle. The retrieved snow emissivity also shows spectral variation and is measurably below 1 between 450 and 900 cm^{-1}. This shows that the assumption made by some climate models that snow emissivity is 1 or a constant value is not realistic. Using the Chen et al. (2014) model for snow emissivity it was not possible to find a set of model parameters that led to a match between the measured and modeled emissivity within the retrieval uncertainty across the whole spectral range. The lack of sufficient independent measurements of the snow properties means that this difference can not be investigated further in this publication. The emissivity predicted by the Chen et al. (2014) model is also independent of the snow skin temperature however, the ice refractive indices that are one of the inputs to the model are weakly dependent on the temperature. Therefore, further work is needed to complete a rigorous comparison between measured snow emissivity in the far-infrared and this widely used emissivity model.

This evaluation should be performed by measuring snow emissivity over a greater range of snow grain sizes, densities, temperatures, and viewing angles than was possible during the Andøya campaign. The uncertainty levels of the emissivity retrievals shown in this paper are sufficient to differentiate between the emissivity of fine and coarse snow (Chen et al., 2014, Figure 2) showing the more extensive measurements from FINESSE would be suitable for performing this evaluation. This should also involve an improved method for measuring the size of the snow crystals. One possibility is to use an instrument designed to measure the snow specific surface area with greater accuracy and precision. Snow specific surface area is the surface area to volume ratio of a snow crystal and can be used as an input into the snow emissivity model. Delivering a fully observationally validated model which links the microphysical properties of snow to its radiative properties in the far-infrared is vital for accurate modeling of the climate and for successful atmospheric retrievals from the PREFIRE and FORUM satellites.

Data Availability Statement

The FINESSE data from the Andøya campaign can be accessed from the European Space Agency Earth Online website: https://doi.org/10.57780/esa-e8a8e82. ERA5 hourly data on pressure levels can be downloaded from the Copernicus Climate Data Store: https://doi.org/10.24381/cds.bd0915c6.

Acknowledgments
LW was funded through an Internal Research Fellowship at the European Space Agency. JM and HB were funded by the Natural Environment Research Council, UK as part of their support for the National Centre for Earth Observation under Grant NE/Y006216/1. SP was funded by the Natural Environment Research Council, UK via the Science and Solutions for a Changing Planet Doctoral Training Partnership. The Andøya Field Campaign was funded by the European Space Agency as part of the FORUM project. The authors would like to thank the MC2-ICEPACKS team for their generous assistance during the campaign including advice about the snow measurements and the loan of the equipment for photographing the snow. The MC2-ICEPACKS campaign was funded by the European Research Council StG 758005 (Mixed-Phase Clouds and Climate) and CoG 101045273 (STEP-CHANGE), EEA Grants/Norway Grants (Grant EEARO-NO-2019-0423/IceSafari, contract no. 31/2020), and EU-HORIZON-WIDERA-2021 (Grant 101079385 (BRACE-MY)). We would also like to thank the team at the ALMOAR Observatory and Andøya Space, particularly Reidar Lyngra and Martin Flügge, for their help throughout the campaign. LW would like to thank Elena Favero, Research Fellow at ESA-ESTEC, for her help analyzing the snow photographs.

References

Bellisario, C., Brindley, H. E., Murray, J. E., Last, A., Pickering, J., Harlow, R. C., et al. (2017). Retrievals of the far infrared surface emissivity over the Greenland Plateau using the Tropospheric Airborne Fourier Transform Spectrometer (TAFTS). *Journal of Geophysical Research: Atmospheres*, *122*(22), 12152–12166. https://doi.org/10.1002/2017JD027328

Ben-Yami, M., Oetjen, H., Brindley, H., Cossich, W., Lajas, D., Maestri, T., et al. (2022). Emissivity retrievals with FORUM's end-to-end simulator: Challenges and recommendations. *Atmospheric Measurement Techniques*, *15*(6), 1755–1777. https://doi.org/10.5194/amt-15-1755-2022

Borbas, E. E., Adler, D. P., Best, F. A., Knuteson, R. O., L'Ecuyer, T. S., Loveless, M., et al. (2021). Ground-based far-infrared emissivity measurements with the University of Wisconsin absolute radiance interferometer (ARI). In M. Strojnik (Ed.), *Infrared remote sensing and instrumentation XXIX* (Vol. 11830). SPIE. https://doi.org/10.1117/12.2594834.1183004

Chen, X., Huang, X., & Flanner, M. G. (2014). Sensitivity of modeled far-IR radiation budgets in polar continents to treatments of snow surface and ice cloud radiative properties. *Geophysical Research Letters*, *41*(18), 6530–6537. https://doi.org/10.1002/2014GL061216

Clough, S., Shephard, M., Mlawer, E., Delamere, J., Iacono, M., Cady-Pereira, K., et al. (2005). Atmospheric radiative transfer modeling: A summary of the AER codes. *Journal of Quantitative Spectroscopy and Radiative Transfer*, *91*(2), 233–244. https://doi.org/10.1016/j.jqsrt.2004.05.058

EUMETSAT. (2017). IASI level 2: Product guide. Document number: EUM/OPS-EPS/MAN/04/0033. Issue: v3E e-signed. Retrieved from https://user.eumetsat.int/s3/eup-strapi-media/IASI_Level_2_Product_Guide_8f61a2369f.pdf

European Space Agency. (2024). FINESSE at Andøya campaign [Dataset]. https://doi.org/10.57780/esa-e8a8e82

Feldman, D. R., Collins, W. D., Pincus, R., Huang, X., & Chen, X. (2014). Far-infrared surface emissivity and climate. *Proceedings of the National Academy of Sciences of the United States of America*, *111*(46), 16297–16302. https://doi.org/10.1073/pnas.1413640111

Fiedler, L., & Bakan, S. (1997). Interferometric measurements of sea surface temperature and emissivity. *Deutsche Hydrografische Zeitschrift*, *49*(2), 357–365. https://doi.org/10.1007/BF02764044

Hapke, B. (1993). *Theory of reflectance and emittance spectroscopy*. Cambridge University Press. https://doi.org/10.1017/CBO9780511524998

Hersbach, H., Bell, B., Berrisford, P., Biavati, G., Horányi, A., Muñoz Sabater, J., et al. (2023). ERA5 hourly data on pressure levels from 1940 to present. *(Copernicus Climate Change Service (C3S) Climate Data Store (CDS)*. https://doi.org/10.24381/cds.bd0915c6

Hori, M., Aoki, T., Tanikawa, T., Motoyoshi, H., Hachikubo, A., Sugiura, K., et al. (2006). In-situ measured spectral directional emissivity of snow and ice in the 8–14 μm atmospheric window. *Remote Sensing of Environment*, *100*(4), 486–502. https://doi.org/10.1016/j.rse.2005.11.001

Huang, X., Chen, X., Zhou, D. K., & Liu, X. (2016). An observationally based global band-by-band surface emissivity dataset for climate and weather simulations. *Journal of the Atmospheric Sciences*, *73*(9), 3541–3555. https://doi.org/10.1175/JAS-D-15-0355.1

Langsdale, M. F., Dowling, T. P. F., Wooster, M., Johnson, J., Grosvenor, M. J., de Jong, M. C., et al. (2020). Inter-comparison of field- and laboratory-derived surface emissivities of natural and manmade materials in support of land surface temperature (LST) remote sensing. *Remote Sensing*, *12*(24), 4127. https://doi.org/10.3390/rs12244127

L'Ecuyer, T. S., Drouin, B. J., Anheuser, J., Grames, M., Henderson, D. S., Huang, X., et al. (2021). The polar radiant energy in the far infrared experiment: A new perspective on polar longwave energy exchanges. *Bulletin of the American Meteorological Society*, *102*(7), E1431–E1449. https://doi.org/10.1175/BAMS-D-20-0155.1

Liang, S., Wang, D., He, T., & Yu, Y. (2019). Remote sensing of Earth's energy budget: Synthesis and review. *International Journal of Digital Earth*, *12*(7), 737–780. https://doi.org/10.1080/17538947.2019.1597189

Loveless, M., Adler, D., Best, F., Borbas, E., Huang, X., Knuteson, R., et al. (2024). Ground-based far infrared emissivity measurements using the absolute radiance interferometer. *Earth and Space Science*, *11*(7), e2024EA003574. https://doi.org/10.1029/2024EA003574

Masuda, K., Takashima, T., & Takayama, Y. (1988). Emissivity of pure and sea waters for the model sea surface in the infrared window regions. *Remote Sensing of Environment*, *24*(2), 313–329. https://doi.org/10.1016/0034-4257(88)90032-6

Meerdink, S. K., Hook, S. J., Roberts, D. A., & Abbott, E. A. (2019). The ECOSTRESS spectral library version 1.0. *Remote Sensing of Environment*, *230*, 111196. https://doi.org/10.1016/j.rse.2019.05.015

Mishchenko, M. I. (1994). Asymmetry parameters of the phase function for densely packed scattering grains. *Journal of Quantitative Spectroscopy and Radiative Transfer*, *52*(1), 95–110. https://doi.org/10.1016/0022-4073(94)90142-2

Mishchenko, M. I., & Macke, A. (1997). Asymmetry parameters of the phase function for isolated and densely packed spherical particles with multiple internal inclusions in the geometric optics limit. *Journal of Quantitative Spectroscopy and Radiative Transfer*, *57*(6), 767–794. https://doi.org/10.1016/S0022-4073(97)00012-5

Murray, J., Brindley, H. E., Fox, S., Bellisario, C., Pickering, J. C., Fox, C., et al. (2020). Retrievals of high-latitude surface emissivity across the infrared from high-altitude aircraft flights. *Journal of Geophysical Research: Atmospheres*, *125*(22), e2020JD033672. https://doi.org/10.1029/2020JD033672

Murray, J., Warwick, L., Brindley, H., Last, A., Quigley, P., Rochester, A., et al. (2024). The far-infrared spectrometer for surface emissivity (FINESSE) – Part 1: Instrument description and level 1 radiances. *Atmospheric Measurement Techniques*, *17*(16), 4757–4775. https://doi.org/10.5194/amt-17-4757-2024

Newman, S. M., Smith, J. A., Glew, M. D., Rogers, S. M., & Taylor, J. P. (2005). Temperature and salinity dependence of sea surface emissivity in the thermal infrared. *Quarterly Journal of the Royal Meteorological Society*, *131*(610), 2539–2557. https://doi.org/10.1256/qj.04.150

Palchetti, L., Barucci, M., Belotti, C., Bianchini, G., D'Amato, F., Di Natale, G., et al. (2020). FIRMOS D8 final report. ESA Contract No. 4000123691/18/NL/LF. Retrieved from https://earth.esa.int/eogateway/documents/20142/37627/FIRMOS-D8-final-report-v3.6.pdf

Palchetti, L., Brindley, H., Bantges, R., Buehler, S. A., Camy-Peyret, C., Carli, B., et al. (2020). FORUM: Unique far-infrared satellite observations to better understand how Earth radiates energy to space. *Bulletin of the American Meteorological Society*, *101*(12), E2030–E2046. https://doi.org/10.1175/BAMS-D-19-0322.1

Salisbury, J. W., & D'Aria, D. M. (1992). Emissivity of terrestrial materials in the 8–14 μm atmospheric window. *Remote Sensing of Environment*, *42*(2), 83–106. https://doi.org/10.1016/0034-4257(92)90092-X

10.1029/2025EA004350

Salvaggio, C., & Miller, C. J. (2001). Comparison of field- and laboratory-collected midwave and longwave infrared emissivity spectra/data reduction techniques. In S. S. Shen & M. R. Descour (Eds.), *Algorithms for multispectral, hyperspectral, and ultraspectral imagery VII* (Vol. 4381, pp. 549–558). SPIE. https://doi.org/10.1117/12.437047

Schaepman-Strub, G., Schaepman, M., Painter, T., Dangel, S., & Martonchik, J. (2006). Reflectance quantities in optical remote sensing—Definitions and case studies. *Remote Sensing of Environment*, *103*(1), 27–42. https://doi.org/10.1016/j.rse.2006.03.002

Smith, W. L., Knuteson, R. O., Revercomb, H. E., Feltz, W., Howell, H. B., Menzel, W. P., et al. (1996). Observations of the infrared radiative properties of the ocean–implications for the measurement of sea surface temperature via satellite remote sensing. *Bulletin of the American Meteorological Society*, *77*(1), 41–52. https://doi.org/10.1175/1520-0477(1996)077⟨0041:OOTIRP⟩2.0.CO;2

Wang, S., Ren, T., Yang, P., Saito, M., & Brindley, H. E. (2024). Improved temperature-dependent ice refractive index compilation in the far-infrared spectrum. *Geophysical Research Letters*, *51*(14), e2024GL110176. https://doi.org/10.1029/2024GL110176

Warren, S. G., & Brandt, R. E. (2008). Optical constants of ice from the ultraviolet to the microwave: A revised compilation. *Journal of Geophysical Research*, *113*(D14), D14220. https://doi.org/10.1029/2007JD009744

Warwick, L., Murray, J. E., & Brindley, H. (2024). The Far-INfrarED Spectrometer for Surface Emissivity (FINESSE) – Part 2: First measurements of the emissivity of water in the far-infrared. *Atmospheric Measurement Techniques*, *17*(16), 4777–4787. https://doi.org/10.5194/amt-17-4777-2024

Wild, M., Folini, D., Hakuba, M. Z., Schär, C., Seneviratne, S. I., Kato, S., et al. (2015). The energy balance over land and oceans: An assessment based on direct observations and CMIP5 climate models. *Climate Dynamics*, *44*(11–12), 3393–3429. https://doi.org/10.1007/s00382-014-2430-z

Xie, Y., Huang, X., Chen, X., L'Ecuyer, T. S., Drouin, B. J., & Wang, J. (2022). Retrieval of surface spectral emissivity in polar regions based on the optimal estimation method. *Journal of Geophysical Research: Atmospheres*, *127*(5), e2021JD035677. https://doi.org/10.1029/2021JD035677